Journal of Energy Storage 63 (2023) 107015

Contents lists available at ScienceDirect

Journal of Energy Storage

journal homepage: www.elsevier.com/locate/est

Research Papers

# New insights into the heat capacity enhancement of nano-$SiO_2$ doped alkali metal chloride molten salt for thermal energy storage: A molecular dynamics study

Xueming Yang [a,*], Chang Ji [a], Jieting Liu [a,b], YongFu Ma [a], Bingyang Cao [c,*]

[a] Hebei Key Laboratory of Low Carbon and High Efficiency Power Generation Technology, Department of Power Engineering, North China Electric Power University, Baoding 071003, China
[b] Department of Power Engineering, Harbin Electric Power Vocational and Technical College, Harbin 150030, China
[c] Key Laboratory for Thermal Science and Power Engineering of Ministry of Education, Department of Engineering Mechanics, Tsinghua University, Beijing 100084, China

ARTICLE INFO

*Keywords:*
Molten salt
Nanoparticles
Nanofluids
Molecular dynamics
Buckingham potential

ABSTRACT

Molten salts and their based nanofluids are important media for heat transfer and thermal energy storage in concentrated solar power (CSP) system. To improve the overall efficiency of the CSP plants, it is important to increase the specific heat capacity of molten salt to the extent possible. Nanomaterials have been doped in molten salt to enhance the specific heat capacity of molten salt; however, the mechanism of enhancement in specific heat capacity caused by doping of nanoparticles in molten salt is still unclear. In this work, the Buckingham force field parameters for alkali metal chloride molten salts (KCl, NaCl, LiCl) were first derived and carefully validated. The specific heat capacities, viscosities, and self-diffusion coefficients of pure molten salts and the specific heat capacities of molten-salt-based nanofluids with $SiO_2$ nanoparticles were investigated by molecular dynamics (MD) simulations. The calculated thermophysical properties of the chloride molten salts using the derived Buckingham potential parameters are in good agreement with the experimental data, and the overall prediction performance is better than that of the BMH potential. Results show that the specific heat capacity of molten salt first increases and then decreases with increasing $SiO_2$ doping ratio, reaching a maximum value at 1 wt%. The specific heat capacities of KCl, NaCl and LiCl nanofluids with 1 wt% $SiO_2$ nanoparticle are increased by 6.2 %, 8.6 % and 19.8 % compared to the base salts, respectively. Number density, radial distribution function, coordination number curves, and energy of the nanofluid system were systematically analyzed. It is found that the increase of the specific heat capacities of the molten salt-based nanofluids can be explained by the energy and coordination number change caused by the number density mismatch of cations and anions. Interestingly, the local delamination of cations around $SiO_2$ nanoparticle surfaces in LiCl-$SiO_2$ nanofluids is clearly observed and visualized for the first time; it is a phenomenon well explained by the analysis of number density and contributes to the further enhancement of the heat capacity. The findings of this work could provide important fundamentals in understanding and designing more efficient molten salt nanocomposites for thermal energy storage in future studies.

## 1. Introduction

Concentrated solar power technology (CSP) is increasingly important [1], and molten salt has been used as thermal energy storage (TES) and heat transfer material in CSP [2–6]. Compared with traditional heat transfer substances such as oil and steam, molten salt has many useful properties, including large specific heat capacity, high thermal stability, low cost, low pressure, and negligible toxicity. Studies of chloride molten salt as a high-temperature heat storage material and a heat transfer medium for CSP have been reported [7–9]. For engineering applications, the most important property of molten salt is its specific heat capacity [10]. It is therefore important to increase the specific heat capacity of molten salt to the extent possible.

To enhance the specific heat capacity of molten salt, nanomaterials have been doped in molten salt [11,12]. Tiznobaik et al. [13] doped 1 wt % of $SiO_2$ nanoparticles in the mixed salt of $K_2CO_3$ and $Li_2CO_3$ (molar

* Corresponding authors.
*E-mail addresses:* xuemingyang@ncepu.edu.cn (X. Yang), caoby@tsinghua.edu.cn (B. Cao).

https://doi.org/10.1016/j.est.2023.107015
Received 2 January 2023; Received in revised form 6 February 2023; Accepted 27 February 2023

ratio 38:62), and found the specific heat capacity of the mixed salt to be increased by 25 %. Lai et al. [14] increased the specific heat capacity of HITEC salt by 30 % by doping 5 wt% $Sn/SiO_2$ core-shell in it. Ho et al. [15] doped HITEC salt with 0.063 wt% $Al_2O_3$, and found the specific heat capacity of HITEC salt to be increased by 19.9 %. Dudda et al. [16] doped solar salt with $SiO_2$ nanoparticles with a doping ratio of 1 wt% and with different nanoparticles sizes (5, 10, 30, and 60 nm). They found that the $SiO_2$ nanoparticles with a diameter of 60 nm had the greatest impact on the solar salt's specific heat capacity, increasing it by 27 %. Shin et al. [17] doped 1 wt% $SiO_2$ nanoparticles in a quaternary mixed chloride molten salt ($BaCl_2$, NaCl, $CaCl_2$, LiCl), which resulted in a 14.5 % increase in specific heat capacity. Such an increase in specific heat capacity of molten salts doped with nanofluids contradicts the result calculated from a theoretical formula for mixtures as follows [18]:

$$C_{p,mixture} = \frac{m_p C_{p,p} + m_f C_{p,f}}{m_p + m_f} \tag{1}$$

where $C_{p,\ mixture}$ is the specific heat capacity of the mixture, $C_{p,\ p}$ is the specific heat capacity of the nanoparticles, $C_{p,\ f}$ is the specific heat capacity of the molten salt, $m_p$ is the mass of the nanoparticles, and $m_f$ is the mass of the molten salt. At present, some mechanisms have been proposed to explain this phenomenon such as compressed liquid layer [11], Brownian motion of nanoparticles [12], aggregation of nanoparticles [15], nanostructures formed in the nanomaterials [16], effect of specific surface energy, semi-solid liquid layer [17], etc. However, the mechanism of a change in specific heat capacity caused by doping of nanoparticles in molten salt is not fully understood.

As an effective tool, molecular dynamics (MD) simulation has been widely used in the investigation of thermodynamic properties and microscopic mechanisms of fluids such as molten salt [19,20], fuels [21], and other mixtures [22,23]. Anagnostopoulos et al. [24] predicted the density, thermal conductivity, self-diffusion coefficient, shear viscosity, and surface tension of $KNO_3$ and $NaNO_3$ using MD simulation, and reported that the differences between their simulation results and measured properties were all below 10 %. Ding et al. [25] simulated the thermophysical properties of molten alkali carbonate $K_2CO_3$—including density, thermal expansion coefficient, specific heat capacity, shear viscosity, thermal conductivity, and ion self-diffusion coefficient—at 1200–1600 K. Pan et al. [26] used the reverse non-equilibrium MD (RNEMD) method to simulate the shear viscosity and thermal conductivity of the molten salt of alkali metal chlorides, and got results basically consistent with experimental data, with differences of 5.2 % and 17.1 %, respectively. In terms of molten salt nanofluid, Hu et al. [27] performed MD simulations on the specific heat capacity of a nanofluid of binary nitrate eutectic salt doped with $SiO_2$. They reported that the specific heat capacity of solar salt increased the most when the doping ratio of $SiO_2$ nanoparticles was 1 wt%, which is consistent with their experimental results. Jo et al. [28] used molecular dynamics to simulate the specific heat capacity of binary carbonate ($K_2CO_3 + Li_2CO_3$) doped with carbon nanotubes and found that the increase of specific heat capacity is related to a compressed liquid layer formed in the solvent near the nanoparticles.

To date there have been only very few MD studies of alkali metal chloride molten salt doped with oxide nanoparticles; this is because of a lack of suitable potential functions with which to accurately describe the interactions of both the alkali metal chlorides and oxide. Yu et al. [29], using the COMPASS force field, simulated the thermophysical properties (excluding specific heat capacities) of NaCl-based $SiO_2$ nanofluids. However, this force field gave large errors in describing thermophysical properties such as melting point, density, and viscosity near the melting point of NaCl. Moreover, COMPASS force field is not a freely available force-field, it is in an encrypted database of the Materials Studio software. There are currently two main forms of potential used in simulating ionic solids, the Born-Mayer-Huggins (BMH) potential [30] and the Buckingham potential [31,32]. The Buckingham potential is the most commonly used potential for describing atomic interactions in ionic materials [33], and is suitable for the vast majority of oxides, e.g., $Al_2O_3$, $Fe_2O_3$, $TiO_2$, ZnO [34], and crystalline $SiO_2$ [35]. However, it has some difficulty in MD simulation of alkali metal chloride molten salt due to the lack of corresponding potential parameters. In contrast, the BMH potential can well simulate alkali metal chlorides molten salt, however it was reported that it is only suitable for an amorphous state of $SiO_2$ rather than crystalline $SiO_2$ [36]. In this paper, the Buckingham potential parameters for alkali metal chloride molten salt are derived and validated, and thermodynamic properties of alkali metal chloride molten salt are calculated via MD simulations. Also, specific heat capacities of chloride molten salt-silica nanofluid are predicted and mechanisms of increasing the specific heat capacity of nano-$SiO_2$ on alkali metal chloride molten salt are analyzed.

## 2. Methodology

### 2.1. Force field

In this work, the Buckingham potential with Coulomb interaction is used for the alkali metal chloride molten salt, and the parameters of the Buckingham potential are calculated from the parameters of the BMH pair potential. The expressions of BMH potential [37] and Buckingham potential [32] are as follows:

$$U_{ij}^{BMH} = \frac{q_i q_j}{r_{ij}} + A_{ij}^{BMH} exp\left(\frac{\sigma_{ij} - r_{ij}}{\rho}\right) - \frac{C_{ij}^{BMH}}{r_{ij}^6} - \frac{D_{ij}^{BMH}}{r_{ij}^8} \tag{2}$$

$$U_{ij}^{BUCK} = \frac{q_i q_j}{r_{ij}} + A_{ij}^{BUCK} exp\left(\frac{-r_{ij}}{\rho}\right) - \frac{C_{ij}^{BUCK}}{r_{ij}^6} \tag{3}$$

where the formal charges $q_i$ and $q_j$ can be +1 (alkali metal ion) or −1 (chloride ion); $r_{ij}$ is the distance between two ion centers; $A_{ij}^{BMH}$ and $A_{ij}^{BUCK}$ are, respectively, the repulsion parameters in the BMH potential and the Buckingham potential; $\sigma_{ij} = \sigma_i + \sigma_j$, where $\sigma_i$ and $\sigma_j$ are the ionic radii of the crystal; $\rho$ is the hardness parameter; $C_{ij}^{BMH}$ and $D_{ij}^{BMH}$ are van der Waals parameters in the BMH potential; and $C_{ij}^{BUCK}$ is the van der Waals parameter in the Buckingham potential.

The Buckingham potential can be derived from a BMH potential when $D_{ij}^{BMH}$ is set to zero. In fact, numerous studies using the BMH potential ignored the term $D_{ij}^{BMH}/r_{ij}^8$even the whole dispersion term [38,39]. Gruenhut et al. [40] derived the Buckingham potential for fluoride glasses from a BMH potential, and their work showed that the Buckingham potential can well reproduce fluoride-based simulation by the BMH potential. The input parameters for the BHM potential can be converted into their equivalent Buckingham form as follows,

$$A_{ij}^{BUCK} = A_{ij}^{BMH} exp\left(\frac{\sigma_{ij}}{\rho}\right), \quad C_{ij}^{BMH} = C_{ij}^{BUCK} \tag{4}$$

In this study, the BMH potential parameters for KCl, NaCl, and LiCl are taken from Ref. [37], and the Buckingham potential parameters are taken from Refs. [32,35] in which a validation had been made for $SiO_2$

**Table 1**
Buckingham potential parameters for $SiO_2$, LiCl, NaCl, and KCl.[a]

| Pair | $q_i$(e) | $A_{ii}$(kcal·mol$^{-1}$) | $\rho_{ij}$(Å) | $C_{ii}$(kcal·mol$^{-1}$·Å$^6$) |
|---|---|---|---|---|
| Li-Li | 1 | 1142.28 | 0.342 | 1.051 |
| Na-Na | 1 | 9778.06 | 0.317 | 24.18 |
| K-K | 1 | 36,197.98 | 0.337 | 349.9 |
| O-O | −0.955209 | 15,170.70 | 0.386 | 617.24 |
| Si-Si | 1.910418 | 72,460.64 | 0.351 | 14,415.29 |
| NaCl(Cl-Cl) | −1 | 80,475.21 | 0.317 | 1669.02 |
| KCl(Cl-Cl) | −1 | 44,379.87 | 0.337 | 1791.32 |
| LiCl(Cl-Cl) | −1 | 38,212.20 | 0.342 | 1597.88 |

[a] For the Buckingham potential, the cross-terms were computed using the following mixing rules: $A_{ij} = (A_{ii} \cdot A_{jj})^{1/2}, C_{ij} = (C_{ii} \cdot C_{jj})^{1/2}$, $1/\rho_{ij} = (1/\rho_{ii} + 1/\rho_{jj})/2$.

[35]. The derived values of parameters in the Buckingham potential for KCl, NaCl, and LiCl via Eq. (5) are listed in Table 1.

### 2.2. Simulation details

MD simulations are performed on systems of single-component NaCl, KCl, and LiCl, and on molten alkali chloride salts doped with $SiO_2$ nanoparticles, all using the large-scale atom/molecule massively parallel simulator (LAMMPS) package [41]. As shown in Fig. 1a, the number of atoms in a single-component system is 5000. The modeling process flow of $SiO_2$ nanoparticles doped in alkali metal chloride molten salt is shown in Fig. 1b and c. In the process, a unit cell of $SiO_2$ is first created; then the unit cell is expanded into a cubic crystal with a side length of 20 Å; finally, a cutting program is used to cut the crystal into a spherical structure with a diameter of 1 nm, containing 40 oxygen atoms and 20 silicon atoms. In fact, due to the simulation cost, many MD simulation studies [29,32] on the molten salts nanofluids have chosen 1 nm as the nanoparticle size, in which the conclusion should be suitable for other nanoparticle sizes. This procedure changes the doping ratio of molten salt-based nanofluid by changing the number of $SiO_2$ nanoparticles.

The simulations are carried out in a 3D cubic box with periodic boundary conditions applied along the x-, y- and z-directions. The long-range Coulomb interactions are computed by utilizing the Ewald method [42] with a cutoff distance of 20 Å and an accuracy of $10^{-6}$. In the MD simulations, the simulation system was first heated to 1600 K and then cooled to desired temperatures; then, the system was equilibrated in the isothermal-isobaric ensemble (NPT) ensemble for 100 million timesteps at corresponding temperature and the atmospheric pressure, and the temperature and stress damping parameters were set to be 100 and 500 fs, respectively. [25] The initial velocities are randomly assigned and obey a Gaussian distribution. The Newtonian equation is solved using the Verlet algorithm, with a time step of 1 fs. When calculating the specific heat capacity, the result is evaluated via NPT ensemble fluctuation [43], and the duration is 1 million time steps [32]. When calculating viscosity, self-diffusion coefficient, mean square displacement, and radial distribution function, the simulations initially run in NPT ensemble to control the pressure and temperature of the system at a given pressure and given temperature for 1 ns; then switch to the NVT ensemble to equilibrate the system at the given temperature for another 1 ns; finally, it is switched to the NVE ensemble, the first 1 ns is performed to relax the system, and next 1 ns is used to compute the properties.

### 2.3. Evaluated properties

#### 2.3.1. Radial distribution functions

The radial distribution function (RDF) is used to describe the liquid structure, which is defined as [44]:

$$g_{\alpha\beta}(r) = \frac{1}{4\pi\rho_\beta r^2}\left[\frac{dN_{\alpha\beta}(r)}{dr}\right] \tag{5}$$

where $\rho_\beta$ is the numerical density of $\beta$ particles, $N_{\alpha\beta}(r)$ is called as the coordination number curve which is the number of $\beta$ particles in a sphere with a radius of $r$ with $\alpha$ particles at the center.

#### 2.3.2. Coordination number

The coordination number ($N_{\alpha\beta}$) is one of the most important parameters for characterizing the local structure. It is the average number of $\beta$-type ions in a sphere with α-type ions as the center and a radius of $r_{min}$ which is the position of the first valley of the RDF. $N_{\alpha\beta}$ can be calculated from RDF using the following equation [44]:

$$N_{\alpha\beta} = 4\pi\rho_\beta \int_0^{r_{\min}} g_{\alpha\beta}(r) r^2 dr \tag{6}$$

#### 2.3.3. Shear viscosity

Shear viscosity is a measure of the ability of the fluid to resist deformation under shear stress. In our study, the Green-Kubo formula [45] and equilibrium molecular dynamics (EMD) simulations were used to calculate the viscosity of the fluid. The viscosity can be calculated by

$$\eta = \frac{1}{k_B T V}\int_0^\infty \langle P_{xy}(0) P_{xy}(t)\rangle dt \tag{7}$$

where $\eta$ is the shear viscosity, $V$ and $T$ are respectively the volume and temperature of the system, and $k_B$ is Boltzmann constant, which is equal to $1.3806504 \times 10^{-23}$ in standard units. The angle bracket $\langle\rangle$ denotes the average value of the autocorrelation function. $P_{xy}(t)$ is the pressure tensor component in the $XY$ direction at time $t$, and its expression is as follows:

$$P_{xy}(t) = \sum_{i=1}^{N}\left[m_i v_{xi} v_{yi} + \frac{1}{2}\sum_{j\neq i} x_{ij} f_y(r_{ij})\right] \tag{8}$$

where $m_i$ is the mass of ion $i$, and $v_{xi}$ and $v_{yi}$ are the velocity components of particle $i$ in the x- and y-directions; $x_{ij}$ is the displacement distance of the $x$ component; and $f_y(r_{ij})$ is the force $f_{ij}$exerted in the $y$ direction by ion

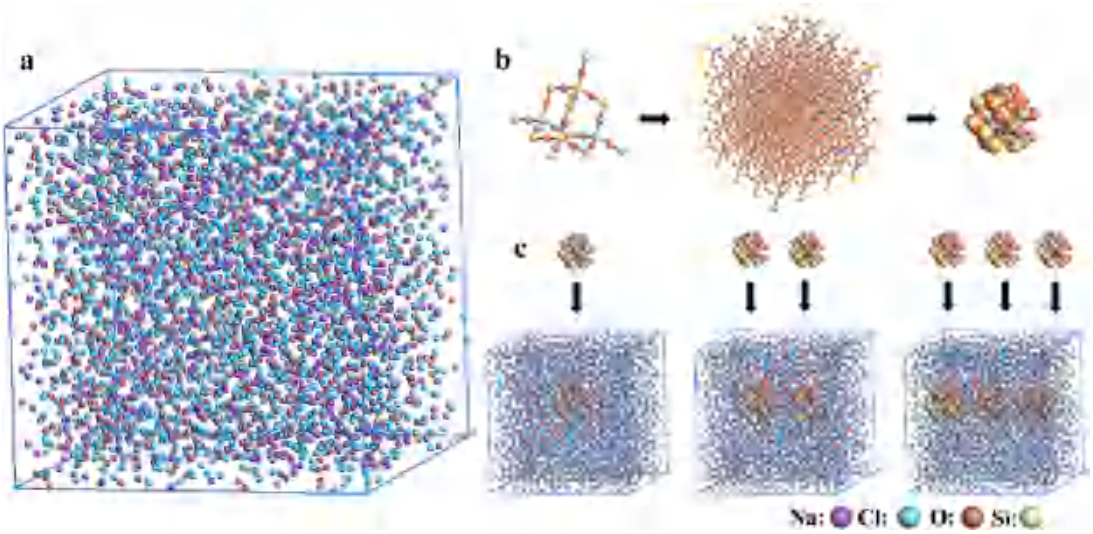


**Fig. 1.** Simulation systems. (a) NaCl. (b) Modeling process of silica nanoparticle. (c) Alkali metal chloride molten salt doped with $SiO_2$ nanoparticles.

$j$ on ion $i$.

#### 2.3.4. Self-diffusion coefficient

According to the Einstein equation [46], the ion self-diffusion coefficient determined by the time-dependent mean square displacement (MSD) can be used to calculate the ion transmission characteristics as follows:

$$D = \frac{1}{6}\frac{dM(t)}{dt} \tag{9}$$

$$M(t) = \left\langle |r_i(t) - r_i(0)|^2 \right\rangle \tag{10}$$

where $M(t)$ is the overall average and $r_i(t)$ is the position of ion $i$.

#### 2.3.5. Specific heat capacity

The specific heat capacity is determined principally by the enthalpy value. Its formula is as follows [47]:

$$C_p = \left(\frac{\partial H}{\partial T}\right)_p \approx \left(\frac{\Delta H}{\Delta T}\right)_p \tag{11}$$

The enthalpy of the system, $H$, is calculated by the following formula:

$$H = U + PV \tag{12}$$

where $U$ is composed of the potential energy and internal energy of the system, representing the total internal energy of the system.

## 3. Results and discussions

### 3.1. Validation of Buckingham potential parameters

In order to verify the reliability of the derived Buckingham potential parameters for chloride molten salts, MD simulations were carried out to calculate the RDFs and thermodynamic properties of three alkali metal chloride molten salts (KCl, NaCl, and LiCl) by using both Buckingham potential and BMH potential. To clarify the comparison and facilitate discussion, the absolute relative errors (AREs) between MD simulation results and experimental data were calculated as $ARE = |A^{sim} - A^{EXP}|/A^{EXP} \times 100\%$, where $A^{sim}$ and $A^{EXP}$ respectively denote the values from MD simulations and experiments.

#### 3.1.1. RDF comparison

RDF is an effective and common way to compare force fields for specific structures at the molecular level. We calculated and compared the RDFs of three alkali metal chloride molten salts using the Buckingham potential with the derived parameters, and compared them with those determined using the BMH potential. Fig. 2a shows the RDFs of ions of KCl, NaCl, and LiCl at a temperature of 1100 K with the Buckingham potential and the BMH potential. It can be seen that the KCl, NaCl, and LiCl structures shown in the RDFs given by the Buckingham potential are in good agreement with those of the BHM potential. Thus, it can be concluded that the Buckingham potential with the derived parameters can reproduce the RDF data obtained by the BMH potential for alkali metal chloride molten salts.

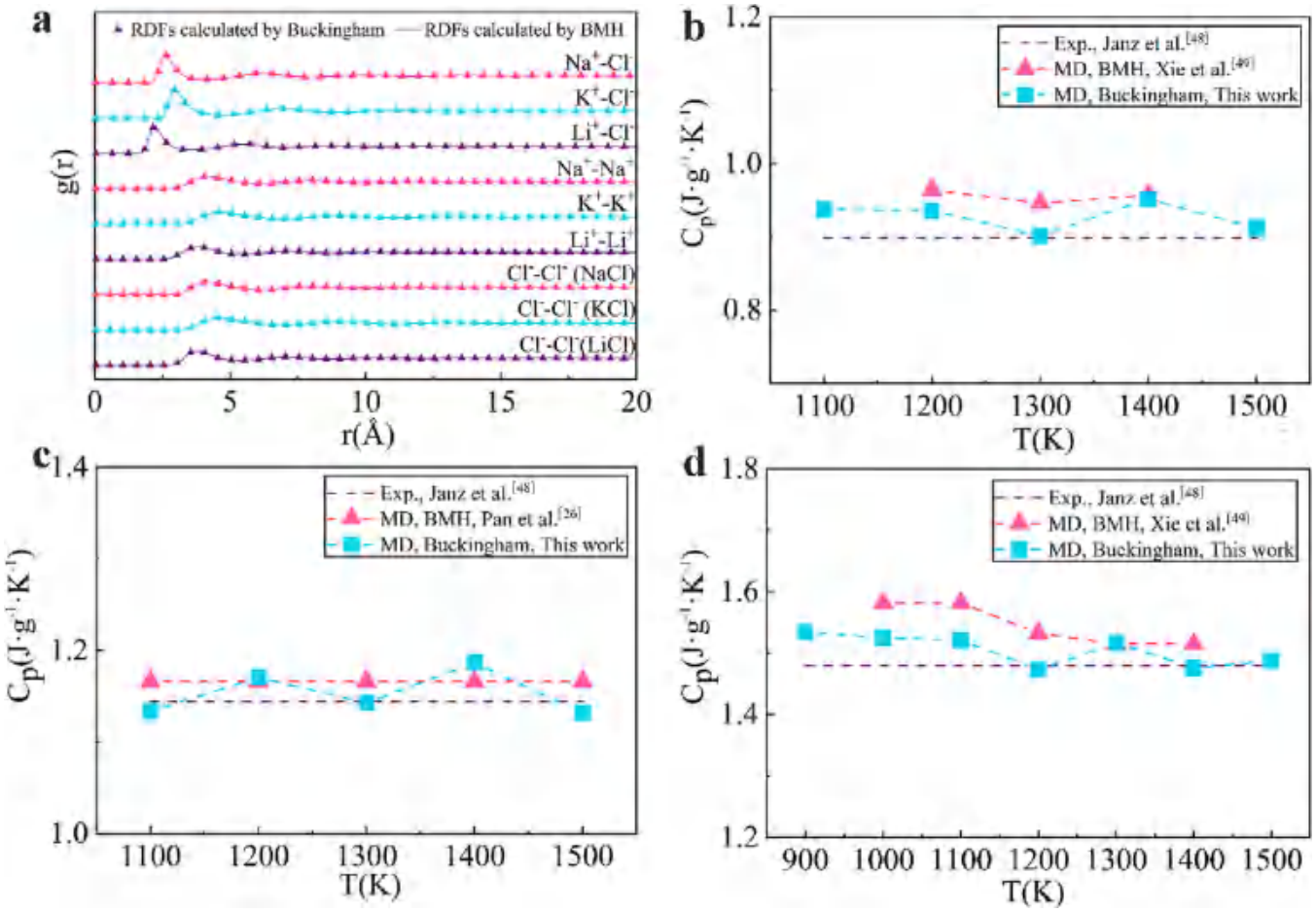


**Fig. 2.** RDFs and specific heat capacities of the pure molten salts. (a) Comparisons of the calculated RDFs using the Buckingham potential and BMH potential. The scatter diagram is for the Buckingham potential and the curve is for the BMH potential. (b) Comparisons of the calculated heat capacities of (b) KCl, (c) NaCl, and (d) LiCl with the reference data at different temperature.

*3.1.2. Simulation of specific heat capacities of KCl, NaCl, and LiCl*

Specific heat capacities of KCl, NaCl, and LiCl were calculated via MD simulations using Eq. (11). The results obtained are shown in Fig. 2. The variations of specific heat capacity of the alkali-metal-chloride molten salts above their melting point are very small. In Fig. 2b,c, and d, the average specific heat capacities of KCl, NaCl, and LiCl in the given temperature range are shown to be 0.93 J/(g·K), 1.15 J/(g·K), and 1.50 J/(g·K), respectively. It can be observed that the simulation results of the three chloride molten salts agree well with the experimental and earlier simulation results. The average *AREs* of the simulation values and experimental data of the specific heat capacity of KCl, NaCl, and LiCl [48] are 3.22 %, 0.79 %, and 1.69 %, respectively, which are less than those using BMH potential in earlier MD studies [26,49] with the average AREs values of 6.34 %,1.91 %, and 4.41 %. This shows that the Buckingham potential is reasonable for calculating the thermophysical properties of the molten state of a chloride.

*3.1.3. Shear viscosity*

Viscosities of KCl, NaCl, and LiCl were calculated via EMD simulations. The strategies of EMD simulations adopted are similar to those in our previous work [50,51]. To overcome the uncertainties of the results using EMD simulations, the viscosity was evaluated by averaging the values for six independent runs of simulations with different initial velocities.

Fig. 3a-c shows, respectively, the calculated values of the viscosities of KCl, NaCl, and LiCl, and their comparisons with experimental data and EMD results using the BMH potential. The total average *ARE* between the simulated and experimental values of all three chloride molten salt viscosities is 3.8 % [52,53]. The average *AREs* of the simulated and experimental values of the individual viscosities of KCl, NaCl, and LiCl are 6.21 %, 0.92 % and 4.53 %, respectively. It can be observed from Fig. 3d that the prediction accuracy of the EMD simulation with the Buckingham potential is better than that with the BMH potential [54]. For example, as shown in Fig. 7(a), the average *ARE* of the viscosity of the EMD simulations with the BMH potential is 12.3 %, which is worse than that of the Buckingham potential with the derived parameters. Moreover, the viscosity of the three chloride molten salts decreases with increasing temperatures. This indicates that an increase of temperature causes an increase of distance between ions and thus reduces the ability of the system to resist shear deformation.

*3.1.4. Self-diffusion coefficient*

Fig. 4a, b, and c respectively shows the calculated mean square displacements (MSDs) of ions of $K^+$, $Na^+$, and $Li^+$. Figs. 4d, e, and f show the MSDs of ions of $Cl^-$ in, respectively, KCl, NaCl, and LiCl. It can be observed that the MSDs of the four ions all increase nonlinearly with an increase of temperature. The self-diffusion coefficients can be obtained through the MSD calculated above using Eq. (9). Comparisons of the simulation results of the self-diffusion coefficients of KCl, NaCl, and LiCl with the experimental values [55,56] is shown in Fig. 4g. The total average *AREs* of the self-diffusion coefficient between MD and the experimental values is 6.11 %. In addition, the self-diffusion coefficients of LiCl are the maximum among the three chloride molten salts, followed by KCl and NaCl. The simulated self-diffusion coefficients for each chloride molten salt increase with the temperature. This is because that as the temperature increases, the structure of the molten salt system becomes loose, reducing resistance to the diffusion of ions to the surroundings and promoting the diffusion of ions. Moreover, the trend of self-diffusion coefficients obeys the Stokes-Einstein (S-E) model [57], which can be expressed as: $D = 2K_BT/(\pi C_{SE}\sigma\eta)$, where $\eta$ is the shear viscosity, $T$ is the temperature, $K_B$ is the Boltzmann constant, $\sigma$ is the hydrodynamic diameter, $C_{SE}$ is the S-E coefficient, and $D$ is the self-diffusion coefficient.

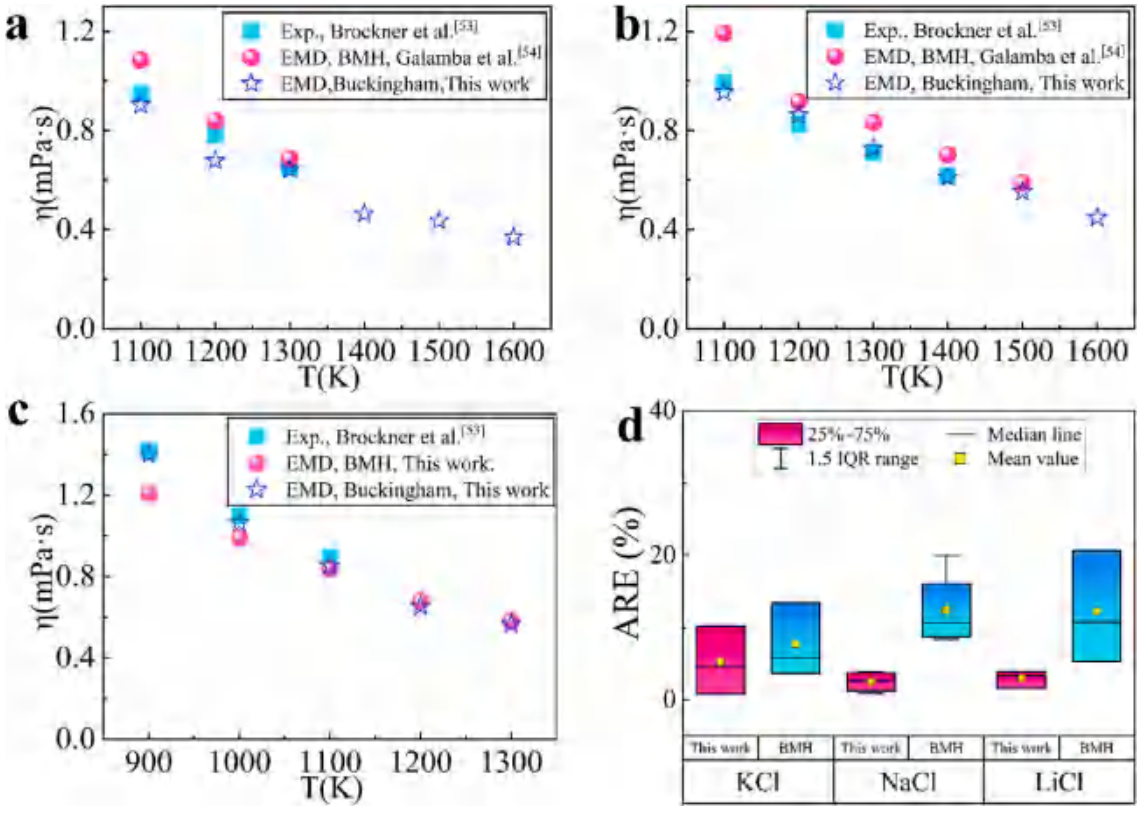


**Fig. 3.** Comparisons of the calculated viscosities at different temperature of (a) KCl, (b) NaCl, and (c) LiCl with the reference data. (d) The average AREs of the calculated viscosities using the Buckingham potential and BMH potential.

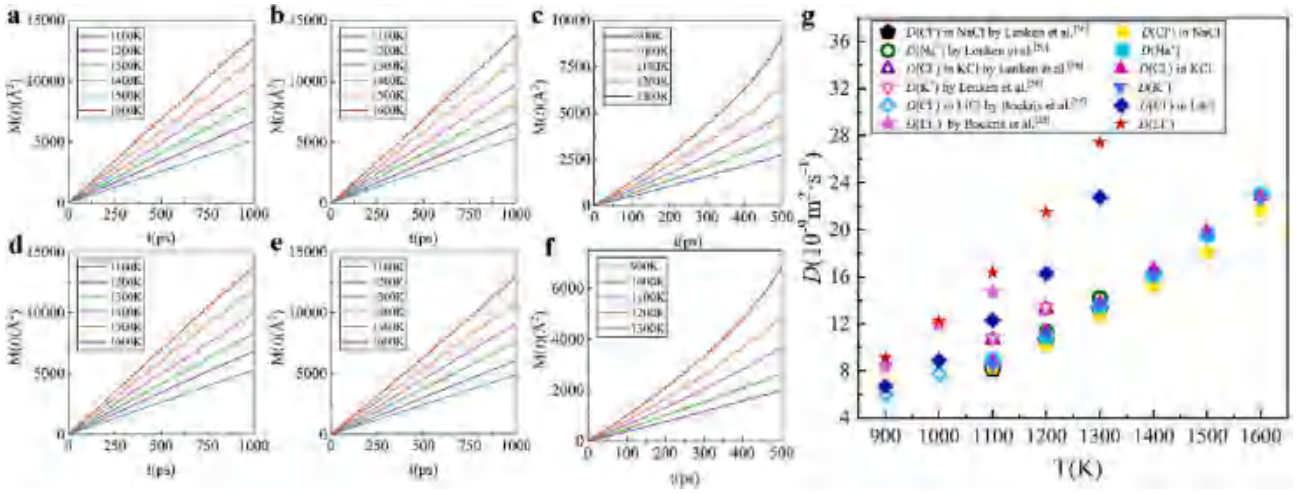

**Fig. 4.** The temperature dependence of the MSDs and self-diffusion coefficients for ions of pure molten salts for (a) $K^+$, (b) $Na^+$, (c) $Li^+$, (d) $Cl^-$ in KCl, (e) $Cl^-$ in NaCl and (f) $Cl^-$ in LiCl. (g) Self-diffusion coefficients of molten KCl, NaCl, and LiCl.

### 3.2. Local structure analysis

The RDFs are calculated to provide a better understanding of the thermophysical properties of alkali metal chloride molten salts at a molecular level. Fig. 5 shows the RDFs of three alkali metal chlorides above the melting point, including the RDF of cation-cation, cation-anion, and anion-anion. The first peak of the RDF of KCl, NaCl, and LiCl is the largest; the peaks of each pure molten salt gradually decrease as distance increases, until they attenuate to about 1.0. This implies that the chloride molten salts above their melting point are characterized by

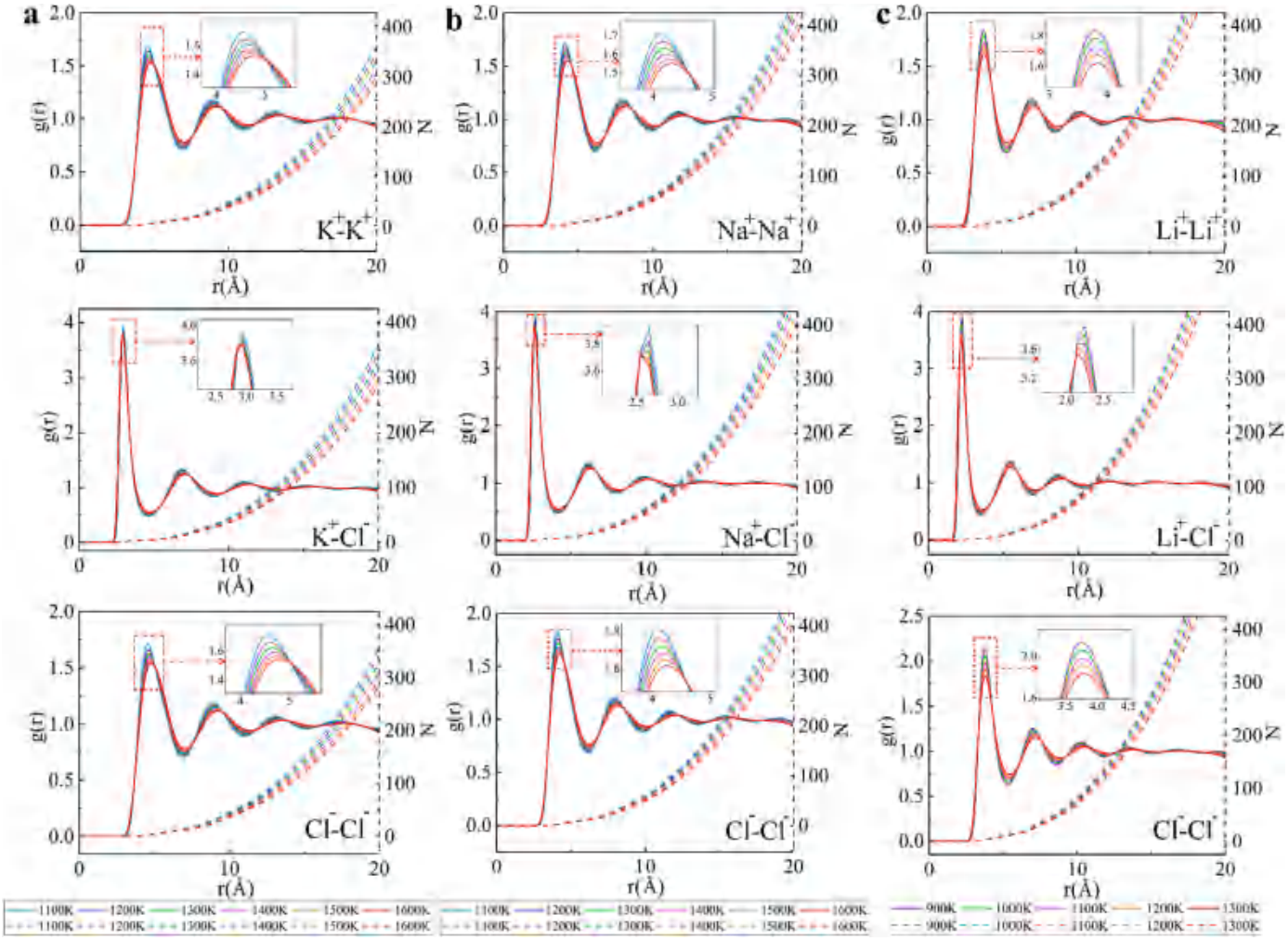

**Fig. 5.** RDFs and the coordination-number curves for (a) KCl, (b) NaCl, and (c) LiCl at different temperatures.

short-range order and long-range disorder.

For different alkali metal chlorides, the positions of the first peaks of the RDF of cation-cation, cation-anion, and anion-anion are different. This indicates that different alkali metal chlorides have different degrees of aggregation at short range. The smaller the $r_{max}$ (the distances of maximum RDF) is, the higher degree of aggregation is. As shown in Fig. 5, at a given temperature, $r_{max}$ of Li-Li in the RDF of cation-cation is the smallest, and $r_{max}$ of K-K is the largest, while the same trend holds for the RDFs of anion-anion. For example, when the temperature is 1100 K, the locations corresponding to the first peaks of the cation-cation RDF of KCl, NaCl, and LiCl are at 4.55 Å, 4.15 Å, and 3.75 Å, respectively. This is in contrast to the trend of the specific heat capacities of the three alkali metal chlorides shown in Fig. 2. These indicate that the shorter the distance between the same ions, the greater the degree of ion aggregation and the higher the value of the specific heat capacity.

The peaks values of the RDF between cation-cation and anion-anion decrease with increasing temperature, and the peaks position moves to the right. The peak values of the RDF between cation and anion also decreases with increasing temperature, but the peak positions shift to the left. This means that the ion-pairs structure of the three alkali metal chlorides changes as the temperature increases. As the temperature increases, the distance between cations and anions becomes shorter, and the distance between ions in the same ion cluster becomes larger. For instance, taking the RDF of Na-Na as an example, as the temperatures increase from 1100 K to 1600 K, and the first peak positions are at 4.15 Å, 4.18 Å, 4.23 Å, 4.25 Å, 4.28 Å, and 4.35 Å, respectively, and the corresponding peak values of RDF are 1.71, 1.67, 1.63, 1.60, 1.57, and 1.54.

Fig. 5 also plots the coordination number curves for three alkali metal chlorides at temperatures above the melting point. It can be seen that the coordination number curves of the three chloride molten salts all decrease with increasing temperature. This indicates that as the temperature increases, the system becomes looser. Moreover, it can be observed that the coordination number of KCl is the most strongly temperature-sensitive among the three chloride molten salts, which indicates that KCl's microstructure is more easily affected by temperature than those of NaCl and LiCl.

The coordination numbers of the three chloride molten salts were then calculated using the coordination number curves and Eq. (6). As shown in Table 2, at the same temperature, K-Cl has the highest coordination number and Li-Cl the smallest. This indicates that under the same conditions, $K^+$ in KCl needs more $Cl^-$ to make the structure stable—that is, LiCl is easier to form a stable ion-pair structure than KCl. Moreover, the coordination number of the three alkali metal chlorides decreases with increasing temperature; it is consistent with the results of the above calculated RDFs, which means that the structure of the molten salt system becomes looser and more disordered with the increasing of temperature.

### 3.3. Analysis of specific heat capacity of molten salt-based nanofluid

#### 3.3.1. Specific heat capacity

By using the Buckingham potential with the derived parameters, specific heat capacities of chloride molten salt-silica nanofluids were calculated and analyzed with MD simulations. The heat capacities are simulated for the KCl-$SiO_2$ and NaCl-$SiO_2$ nanofluids in a temperature range of 1100 K -1600 K and the LiCl-$SiO_2$ nanofluids in a temperature range of 900 K–1300 K, with $SiO_2$-doping ratios of 0.5,1, 2, 3 wt%. It is found that the heat capacities of each molten salt-silica nanofluid vary very little in the investigated temperature ranges, which are similar as those for the three pure molten salts. The average values of predicted specific heat capacities of three kinds of alkali metal chlorides doped with $SiO_2$ nanoparticles in different proportions are shown in Fig. 6a. The results show that the specific heat capacity of a nanofluid is the greatest when the doping ratio of $SiO_2$ nanoparticles is 1 wt%. Doping 1 wt% $SiO_2$ nanoparticles in KCl, NaCl, and LiCl increases the specific heat capacity by 6.2 %, 8.6 %, and 19.8 %, respectively. The specific heat capacities of the KCl-$SiO_2$, NaCl-$SiO_2$ and LiCl-$SiO_2$ nanofluids all increase first and then decrease as the doping ratio increases. This is consistent with the experimental results in ref. [26] showing that the enhancement of the specific heat capacity by doping of $SiO_2$ nanoparticles in solar salt followed a similar trend. However, it should be noted that this result does not obey the mixing law of specific heat capacities in Eq. (1). Moreover, specific heat capacity of the molten salt nanofluids with 0.5 wt% $SiO_2$ added in KCl, NaCl, and LiCl were simulated and investigated. In the simulations, we used the same $SiO_2$ nanoparticle as that in the case of the molten salt nanofluids with 1 wt% $SiO_2$, while the total number of atoms of the molten salt was doubled compared to those of the molten salt nanofluids with 1 wt% $SiO_2$. The results show that the specific heat capacity of KCl, NaCl, and LiCl molten salt nanofluids added with 0.5 wt% $SiO_2$ increases by 2.1 %,3.5 % and 13.6 % compared to those of the base salts, respectively, which is lower than the specific heat capacity of the molten salt nanofluids with 1 wt% $SiO_2$. So far, the mechanism of the changes of specific heat capacity caused by doping of nanoparticles in the molten salt is still not fully understood. Consequently, in the following sections the mechanisms are comprehensively explored and discussed in terms of energy, radial distribution function, coordination number, and number density. Finally, new insights of heat capacity enhancement of nano-$SiO_2$ for alkali metal chloride molten salt: local delamination and number density mismatch of cations and anions, are presented. For convenience in the discussions below, NaCl-$SiO_2$ nanofluid at a temperature of 1100 K is taken as a typical example and described in detail.

**Table 2**
Coordination numbers of alkali metal chlorides at different temperatures.

| T/K | KCl | NaCl | T/K | LiCl |
|---|---|---|---|---|
| 1100 | 5.03 | 4.87 | 900 | 3.98 |
| 1200 | 4.89 | 4.77 | 1000 | 3.91 |
| 1300 | 4.74 | 4.66 | 1100 | 3.83 |
| 1400 | 4.60 | 4.55 | 1200 | 3.75 |
| 1500 | 4.44 | 4.41 | 1300 | 3.65 |
| 1600 | 4.33 | 4.30 | | |

#### 3.3.2. Energy analysis

The system energy of a chloride molten salt-$SiO_2$ nanofluid consists of a kinetic energy part ($E_{kin}$) and a potential energy part ($E_P$). To analyze the effect of the doping ratio of the $SiO_2$ nanoparticles on energy, the potential energy $E_P$, kinetic energy $E_{kin}$, Van der Waals energy $E_{vdw}$, Coulombic energy $E_{coul}$, and long-range K-space energy $E_{long}$ are calculated and analyzed. As shown in Fig. 6b, as the doping ratio of the $SiO_2$ nanoparticles increases, the kinetic energy, Van der Waals energy, and long-range K-space energy of the system do not change significantly. Therefore, in the molten-salt-based nanofluid, the change in potential energy is caused mostly by the change in Coulombic energy. As the doping ratio increases, the absolute values of potential energy and Coulombic energy in the system first increase and then decrease, reaching maximum values at 1 wt%, which is consistent with the variation law of the specific heat capacities.

#### 3.3.3. RDFs and coordination number curves analysis

The Coulombic force affects the ion arrangement on the surfaces of $SiO_2$ nanoparticles. To analyze the distribution of alkali metal chloride ions on these surfaces, RDF calculations are performed on the NaCl nanofluids doped with different proportions of $SiO_2$ nanoparticles. The results are shown in Fig. 6 c. The magnitudes of the first peaks of the RDF between cation-cation, anion-anion, and anion-cation in the system increase with the increasing of the doping ratio of the $SiO_2$ nanoparticles, but the locations of these first peaks for the ions do not move. Such a RDF analysis of the ions cannot clearly explain the mechanism of change of the specific heat capacity of the molten salt-based nanofluid.

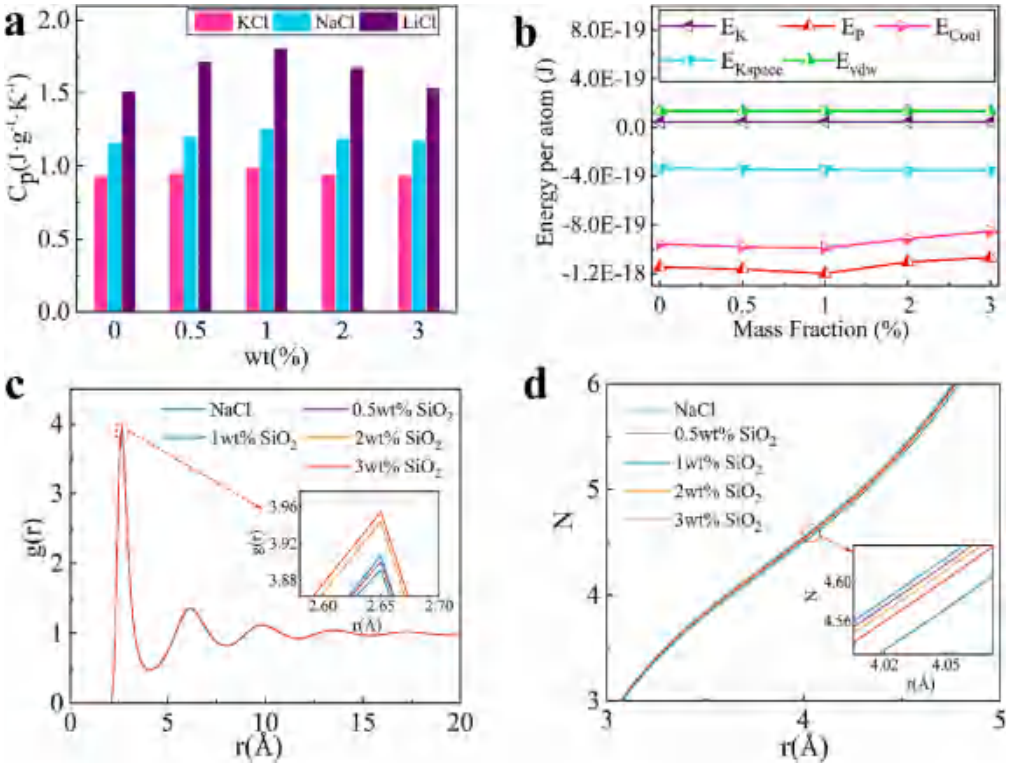


**Fig. 6.** Heat capacity enhancement of nano-$SiO_2$ for alkali metal chloride molten salt and the analysis via energies, RDFs and coordination number curves. (a) The variation of specific heat capacity of the molten salts with the mass fraction of $SiO_2$ nanoparticles. (b) Variation of the energies in NaCl nanofluid with different mass fraction of $SiO_2$ nanoparticles. (c) RDFs for NaCl nanofluids with different mass fraction of $SiO_2$ nanoparticles at 1100 K; (d) Coordination number curves for NaCl nanofluids with different doping ratios of $SiO_2$ nanoparticles at 1100 K.

To extend the analysis, coordination number curves of Na-Cl for the nanofluid at a temperature of 1100 K was calculated, as shown in Fig. 6d. It can be observed that the ordinate value of coordination number curve for NaCl first increases and then decreases as $SiO_2$ doping ratio increases. The coordination number curves reach a maximum value at 1 wt%, then gradually decreases with increasing doping ratio, which coincides with the variation trend of the specific heat capacities. It should be noted that the coordination number of the ions pair Na-Cl in the nanofluid with doped $SiO_2$ is larger than that of pure NaCl at the investigated temperature. This means that the number of ions around a certain ion as the centre is greater in the nanofluid than in pure NaCl. It also suggests that aggregation in the system occurs when doping $SiO_2$ nanoparticles. To clarify such a phenomenon of aggregation, the number densities of ions around the surface of $SiO_2$ nanoparticles were

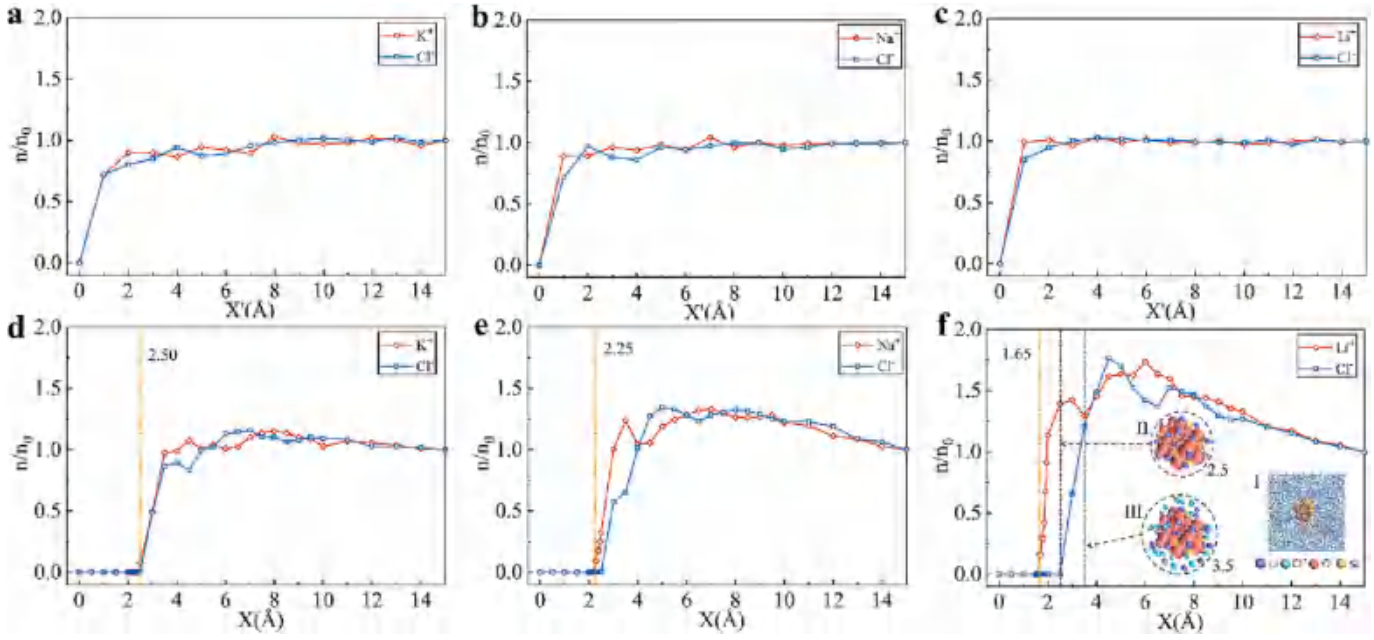


**Fig. 7.** The relative number densities of different systems at a temperature of 1100 K: (a) pure KCl; (b) pure NaCl; (c) pure LiCl; (d) KCl doped with 1 wt% $SiO_2$ nanoparticles; (e) NaCl doped with 1 wt% $SiO_2$ nanoparticles; (f) LiCl doped with 1 wt% $SiO_2$ nanoparticles: (I) Image of the interfacial layer around nanoparticle surface from MD simulation of molten salt-based nanofluid: Subplot (II) ion distribution around nano-$SiO_2$ within a distance of 2.5 Å; Subplot (III) ion distribution around nano-$SiO_2$ within a distance of 3.5 Å.

investigated as discussed in the following subsection.

### 3.3.4. Local delamination and number density mismatch of cations and anions

It should be noted that $SiO_2$ nanoparticles occupy only a small proportion of the doped system and RDF corresponds to the overall degree of aggregation in the system. Therefore, to analyze the local aggregation around the $SiO_2$ nanoparticles, we also performed statistical calculations on the ions around a $SiO_2$ nanoparticle. Here the surface of the $SiO_2$ nanoparticle was used as the starting point to expand outward, and the accumulated number densities of the external space within a distance X from the surface of the nanoparticles were calculated. The number density is the ratio of the number of atoms to the volume. The statistics and calculated results of the relative number density curves for pure molten salts and their doped with 1 wt% nano-$SiO_2$ are compared and shown in Fig. 7. In this figure, $n$ is the accumulated number density corresponding to a distance of X, and $n_0$ is the averaged number density of the system corresponding to the region of X = 0-$X_{max}$ ($X_{max}$ = 15 Å), and $X'$ is the distance from the centre of the system. As shown in Fig. 7a-c, in the three pure molten salt systems at 1100 K, anions and cations are uniformly distributed in the entire system. The statistics and calculated results of the relative number density curves for KCl, NaCl, LiCl doped with 1 wt% nano-$SiO_2$ at 1100 K are shown in Fig. 7d-f.

It can be seen that the addition of nanoparticles changes the microstructure of molten salt around nanoparticles. In the system of KCl, doped with 1 wt% $SiO_2$ nanoparticles, cations appear at 2.5 Å from the surface of $SiO_2$ nanoparticles, and the number density reaches the maximum at 4.5 Å from the surface with a maximum value of 1.10; For NaCl-$SiO_2$ nanofluid, cations appear at 2.25 Å, and the number density peaks of cations locates at 3.5 Å from the surface of the nanoparticle, with a peak value of 1.24; In the system of LiCl, doped with 1 wt% $SiO_2$ nanoparticles, cations appear at 1.65 Å, the cation occurs at 1.65 Å from the surface of the silica nanoparticles and the number density reaches a maximum of 1.42 at the surface 3 Å. It indicates that the position of appearance and the position of first peak of cations are closer to the surface of the nano-$SiO_2$ in the following sequence: KCl-$SiO_2$, NaCl-$SiO_2$ and LiCl-$SiO_2$. Moreover, the value of the first peak of the cations increases in the following sequence: $Na^+ < K^+ < Li^+$. We speculate that this phenomenon may be related to the atomic weight of the cation. The smaller the atomic weight, the more easily the particles are attracted by the nanoparticles, and the compression layer is more obvious, leading to the greater specific heat lift appreciation.

In particular, when LiCl is doped with 1 wt% $SiO_2$ nanoparticle, the anions and cations in the system appear to be obviously delaminated in the interfacial layer around $SiO_2$ nanoparticle. Such a delamination phenomenon images from MD simulation of the interfacial layer around $SiO_2$ nanoparticle surface can be directly observed with VMD software [58], as shown in Fig. 7f. It can be seen from the subplot I of Fig. 7f that no Cl- and only $Li^+$ ions appear around nano-$SiO_2$ within a distance of 2.5 Å. It suggests that the molten salt $Li^+$ are attracted by nanoparticles and form an obvious cationic compression layer. It should be noted that such a delamination phenomenon of the cations in the interfacial layer around $SiO_2$ nanoparticle surface is directly and clearly observed and visualized for the first time.

Fig. 8a-c shows the RDFs of the atoms O and ions of base salt in KCl-$SiO_2$, NaCl-$SiO_2$ and LiCl-$SiO_2$ systems, respectively. The location of the first peaks of O-$K^+$, O-$Na^+$, and O-$Li^+$ are respectively at 3.15 Å, 2.65 Å and 2.00 Å, decreasing successively. This is in line with the conclusions of the analysis by the number densities that the cations are more and more close to the surface of the $SiO_2$ in a sequence of $K^+$, $Na^+$ and $Li^+$ in the three nanofluids system. Moreover, the first peak value of the RDFs for LiCl-$SiO_2$ systems are higher than those for KCl-$SiO_2$ and NaCl-$SiO_2$ systems. It suggests that short-range order and degrees of aggregation are much more pronounced in LiCl-$SiO_2$ systems than those in the KCl-$SiO_2$ and NaCl-$SiO_2$ systems, leading to a more significant enhancement in specific capacity.

The accumulated number densities cannot show the local distribution of the cations and anions directly, therefore the local number density was calculated for the molten salt systems with 1 wt% $SiO_2$ nanoparticle, as shown in Fig. 8d-g. In the figure, $n_L$ is the calculated local number density at a distance of X with an interval 0.5 Å or 1 Å. It can be observed that for KCl-$SiO_2$, NaCl-$SiO_2$, and LiCl-$SiO_2$ nanofluids, the maximum $n_L$ of the ions appears at the layer of cations, with $n_L/n_0$ values of 2.84, 3.27, 3.67, respectively. It is consistent with the increasement of the specific heat capacities of the three nanofluids. In addition, the presence of compressible layers [59–61] around

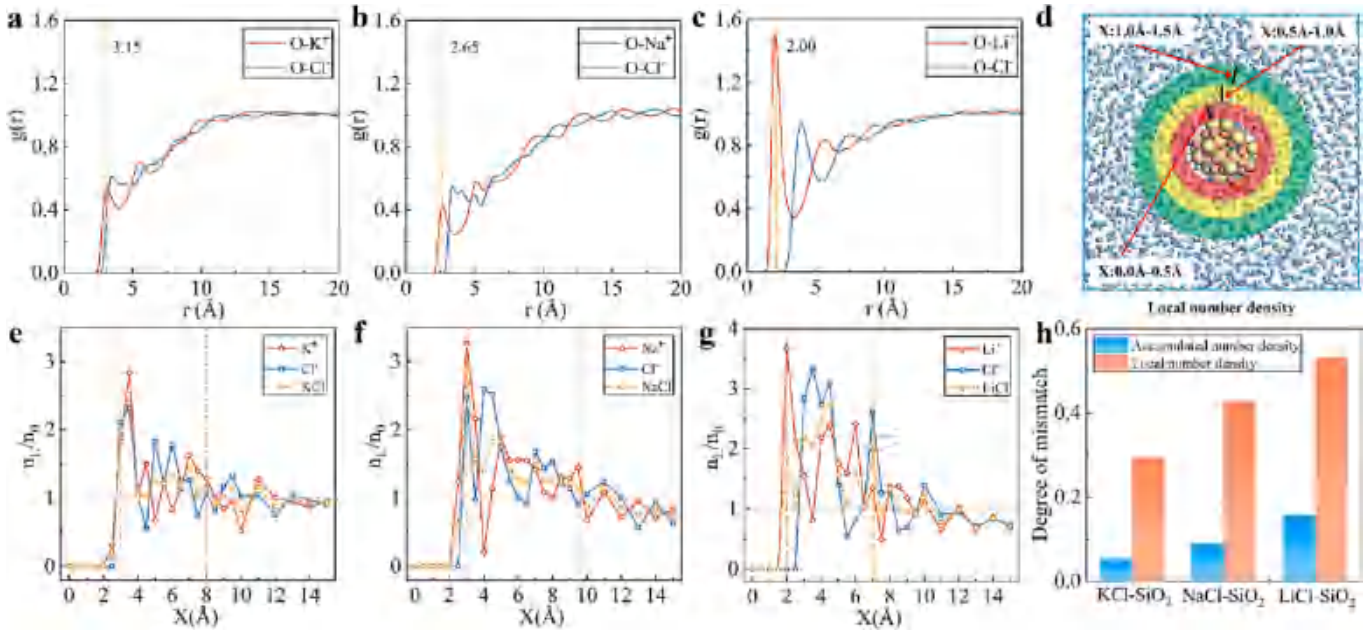


**Fig. 8.** RDFs for NaCl, KCl and LiCl doped with 1 wt% $SiO_2$ nanoparticles at 1100 K: (a) O-K, O-Cl (b) O-Na, O-Cl (c) O-Li, O-Cl (d) Schematic diagram of local number density calculation; The local number densities of different systems at a temperature of 1100 K: (e) KCl doped with 1 wt% $SiO_2$ nanoparticles; (f) NaCl doped with 1 wt% $SiO_2$ nanoparticles. (g) LiCl doped with 1 wt% $SiO_2$ nanoparticles; (h) Calculated mismatch degree.

nanoparticles can be observed more intuitively by local number density curves. The thickness of the compressible layers for the three nanofluids system ranges from 5 to 7.5 Å.

Here we present a new mechanism of an enhancement in specific heat capacity caused by doping of nanoparticles in molten salt, i.e., the mismatch of the relative number densities between the anions and cations in the three systems leads to the phenomenon of enhancement in specific heat capacity. To quantify the analysis of the mismatch of the relative number densities, a mismatch degree of the relative number densities [62] between the anions and cations are calculated as follows.

$$S = \frac{\int |n_+(X) - n_-(X)| dX}{\left( \int n_+(X) dX \int n_-(X) dX \right)^{1/2}} \quad (13)$$

where $S$ is the degree of mismatch in the number density, X is the distance from the surface of the nano-$SiO_2$, $n_+$ is the number density of anions and $n_-$ is the number density of cations.

As shown in Fig. 8h, for the accumulated number densities in Fig. 7d-f, the calculated $S$ for KCl-$SiO_2$, NaCl-$SiO_2$ and LiCl-$SiO_2$ systems is 0.058, 0.089 and 0.156, respectively; while those for the local number densities in Fig. 8e-g are 0.294, 0.429 and 0.532, respectively. The obtained values of the mismatch degree, especially for the accumulated number densities, are better consistent with the increasement of the specific heat capacities of the three nanofluids. Moreover, for the LiCl-$SiO_2$ system, the local delamination of cations around $SiO_2$ nanoparticle surfaces lead to the highest mismatch degree of the relative number densities between the anions and cations, which contribute to the further enhancement of the heat capacity. This indeed illustrates that the heat capacity enhancement of nano-$SiO_2$ for alkali metal chloride molten salt correlate strongly with the mismatch degree of the number densities between the anions and cations.

## 4. Conclusions

In this paper, the Buckingham potential parameters were derived from the BMH potential to describe the interactions in the alkali metal chlorides molten salts. The goal was to make the Buckingham potential suitable for simulating both the chloride molten salts and their oxide-based nanofluids. The Buckingham potential with derived parameters was validated and compared with the BMH potential. The specific heat capacity, viscosity, and self-diffusion coefficient of pure chlorides molten salts (KCl, NaCl, LiCl) were calculated by MD simulations. Results show that the simulated values of the specific heat capacity and self-diffusion coefficient of the three alkali metal chloride molten salts differ from the experimental values by1.90 % and 6.11 %, respectively. The average errors of viscosity of KCl, NaCl, and LiCl molten salts were, respectively, 6.21 %, 0.92 %, and 4.53 %. It was found that the Buckingham potential with derived parameters has better prediction accuracy than BMH potential for the specific heat capacity and shear viscosity of KCl, NaCl, and LiCl.

The specific heat capacities of KCl, NaCl, and LiCl molten salts doped with $SiO_2$ nanoparticles were calculated via MD simulation using the Buckingham potential with the derived parameters. It was found that the specific heat capacities of the molten salts first increase and then decreases with increasing of $SiO_2$ doping ratio, reaching maximum values at 1 wt%. Number density, radial distribution function, and energy of the nanofluids system were analyzed. It was concluded that the increase of the specific heat capacity of the molten salt-based nanofluid can be well explained by the energy change of the nanofluids system and the number density mismatch of cations and anions in the interfacial layer around $SiO_2$ nanoparticle surface. Interestingly, the delamination phenomenon of cations in the interfacial layer around $SiO_2$ nanoparticle surface in LiCl-$SiO_2$ nanofluids is directly and clearly observed and visualized for the first time. The observed delamination agrees well with the results of the analysis of number density. The findings of this work provide deeper insight into the specific heat capacity enhancement of molten salts doped with nanoparticles and should contribute to the design of more efficient molten-salt nanocomposites for thermal energy storage.

## CRediT authorship contribution statement

**Xueming Yang:** Conceptualization, Funding acquisition, Writing – original draft. **Chang Ji:** Formal analysis, Methodology, Investigation, Data curation. **Jieting Liu:** Formal analysis, Investigation, Writing – original draft. **YongFu Ma:** Software, Formal analysis. **Bingyang Cao:** Conceptualization, Supervision, Writing – review & editing.

## Declaration of competing interest

The authors declare that they have no known competing financial interests or personal relationships that could have appeared to influence the work reported in this paper.

## Data availability

Data will be made available on request.

## Acknowledgements

This research is supported by the National Natural Science Foundation of China (Grant No. 52076080) and the Natural Science Foundation of Hebei Province of China (Grant No. E2019502138). This work was carried out at Shanxi Supercomputing Center of China, and the simulations were performed on TianHe-2.

## References

[1] X. Han, L. Wang, H. Ling, Z. Ge, X. Lin, X. Dai, H. Chen, Critical review of thermochemical energy storage systems based on cobalt manganese and copper oxides, Renew. Sust. Energ. Rev. 158 (2022), 112076, https://doi.org/10.1016/j.rser.2022.112076.

[2] Z. Ding, L. Yan, T. Jiang, S. Peng, B. Yue, On the viscosity of molten salts and molten salt mixtures and its temperature dependence, J. Energy Storage 61 (2023), 106707, https://doi.org/10.1016/j.est.2023.106707.

[3] X. Yang, W. Jiang, C. Ji, J.Q. Wang, Experimental study on heat storage and corrosion properties of ternary carbonate salt-based ZnO nanofluids for solar thermal energy storage, Therm. Anal. Calorim. 148 (2022) 1588–2926, https://doi.org/10.1007/s10973-022-11654-4.

[4] L. Sang, X. Lv, Y. Wang, J. Huang, Y. Wu, Investigation of KNO2-KNO3-K2CO3 mixed molten salts with higher working temperature for supercritical CO2 concentrated solar power application, J. Energy Storage 61 (2023), 106724, https://doi.org/10.1016/j.est.2023.106724.

[5] Z. Rong, J. Ding, J. Lu, W. Wang, J. Yan, Experimental and theoretical investigation of an innovative composite nanofluid for solar energy photothermal conversion and storage, J. Energy Storage 52 (2022), 104800, https://doi.org/10.1016/j.est.2022.104800.

[6] M. Akanda, D. Shin, A synthesis parameter of molten salt nanofluids for solar thermal energy storage applications, J. Energy Storage 60 (2023), 106608, https://doi.org/10.1016/j.est.2023.106608.

[7] Y. Li, W. Tie, W. Tan, Q. Zhu, Molecular dynamics simulation of thermophysical properties of NaCl-KCl phase change materials applied to concentrating solar power, J. Energy Storage 52 (2022), 104707, https://doi.org/10.1016/j.est.2022.104707.

[8] W. Ding, T. Bauer, Progress in research and development of molten chloride salt technology for next generation concentrated solar power plants, Engineering 7 (2021) 334–347, https://doi.org/10.1016/j.eng.2020.06.027.

[9] W. Ding, Y. Shi, F. Kessel, D. Koch, T. Bauer, Characterization of corrosion resistance of C/C–SiC composite in molten chloride mixture MgCl2/NaCl/KCl at 700 °C, NPJ Mater. Degrad. 3 (2019) 1–9, https://doi.org/10.1038/s41529-019-0104-3.

[10] L. Ma, Y. Lu, C. Zhang, Y. Wu, Comparative review of different influence factors on molten salt corrosion characteristics for thermal energy storage, Sol. Energy Mater. Sol. Cells 235 (2022), 111485, https://doi.org/10.1016/j.solmat.2021.111485.

[11] P. Bhatnagar, S. Siddiqui, I. Sreedhar, R. Parameshwaran, Molten salts: potential candidates for thermal energy storage applications, Int. J. Energy Res. 46 (2022) 17755–17785, https://doi.org/10.1002/er.8441.

[12] D. Han, B.G. Lougou, Y. Xu, Y. Shuai, X. Huang, Thermal properties characterization of chloride salts/nanoparticles composite phase change material for high-temperature thermal energy storage, Appl. Energy 8 (2013) 448, https://doi.org/10.1016/j.apenergy.2020.114674.

[13] H. Tiznobaik, D. Shin, Enhanced specific heat capacity of high-temperature molten salt-based nanofluids, Int. J. Heat Mass Transf. 57 (2013) 542–548, https://doi.org/10.1016/j.ijheatmasstransfer.2012.10.062.
[14] C.C. Lai, W.C. Chang, W.L. Hu, Z.M. Wang, M.C. Lu, Y.L. Chueh, A solar-thermal energy harvesting scheme: enhanced heat capacity of molten HITEC salt mixed with Sn/SiOx core–shell nanoparticles, Nanoscale 6 (2014) 4555–4559, https://doi.org/10.1039/C3NR06810B.
[15] M.X. Ho, C. Pan, Optimal concentration of alumina nanoparticles in molten hitec salt to maximize its specific heat capacity, Int. J. Heat Mass Transf. 70 (2014) 174–184, https://doi.org/10.1016/j.ijheatmasstransfer.2013.10.078.
[16] B. Dudda, D. Shin, Effect of nanoparticle dispersion on specific heat capacity of a binary nitrate salt eutectic for concentrated solar power applications, Int. J. Therm. Sci. 69 (2013) 37–42, https://doi.org/10.1016/j.ijthermalsci.2013.02.003.
[17] D. Shin, D. Banerjee, Enhancement of specific heat capacity of high-temperature silica-nanofluids synthesized in alkali chloride salt eutectics for solar thermal-energy storage applications, Int. J. Heat Mass Transf. 54 (2011) 1064–1070, https://doi.org/10.1016/j.ijheatmasstransfer.2010.11.017.
[18] O. Alade, M.A.A. Rahman, T.A. Saleh, An approach to predict the isobaric specific heat capacity of nitrides/ethylene glycol-based nanofluids using support vector regression, J. Energy Storage. 29 (2020), 101313, https://doi.org/10.1016/j.est.2020.101313.
[19] L. Du, J. Ding, W. Wang, G. Pan, J. Lu, X. Wei, Molecular dynamics simulations on the binary eutectic system Na2CO3-K2CO3, Energy Procedia 142 (2017) 3553–3559, https://doi.org/10.1016/j.egypro.2017.12.244.
[20] M.F. Costa, Molecular dynamics of molten Li2CO3–K2CO3, J. Mol. Liq. 138 (2008) 61–68, https://doi.org/10.1016/j.molliq.2007.08.001.
[21] X. Yang, Y. Gao, M. Zhang, W. Jiang, B. Cao, Comparison of atomic simulation methods for computing thermal conductivity of n-decane at sub/supercritical pressure, J. Mol. Liq. 342 (2021), 117478, https://doi.org/10.1016/j.molliq.2021.117478.
[22] X. Yang, C. Duan, J. Xu, Y. Liu, B. Cao, A numerical study on the thermal conductivity of H2O/CO2/H2 mixtures in supercritical regions of water for coal supercritical water gasification system, Int. J. Heat Mass Transf. 135 (2019) 413–424, https://doi.org/10.1016/j.ijheatmasstransfer.2019.01.146.
[23] X. Yang, J. Xu, S. Wu, M. Yu, B. Hu, B. Cao, J. Li, A molecular dynamics simulation study of PVT properties for H2O/H2/CO2 mixtures in near-critical and supercritical regions of water, Int. J. Hydrog. Energy 43 (2018) 10980–10990, https://doi.org/10.1016/j.ijhydene.2018.04.214.
[24] A. Anagnostopoulos, A. Alexiadis, Y. Ding, Molecular dynamics simulation of solar salt (NaNO3-KNO3) mixtures, Sol. Energy Mater. Sol. Cells 200 (2019), 109897, https://doi.org/10.1016/j.solmat.2019.04.019.
[25] J. Ding, L. Du, G. Pan, J. Lu, X. Wei, J. Li, W. Wang, J. Yan, Molecular dynamics simulations of the local structures and thermodynamic properties on molten alkali carbonate K2CO3, Appl. Energy 220 (2018) 536–544, https://doi.org/10.1016/j.apenergy.2018.03.116.
[26] G.C. Pan, J. Ding, W. Wang, J. Lu, J. Li, X. Wei, Molecular simulations of the thermal and transport properties of alkali chloride salts for high-temperature thermal energy storage, Int. J. Heat Mass Transf. 103 (2016) 417–427, https://doi.org/10.1016/j.ijheatmasstransfer.2016.07.042.
[27] Y. Hu, Y. He, Z. Zhang, D. Wen, Enhanced heat capacity of binary nitrate eutectic salt-silica nanofluid for solar energy storage, Sol. Energy Mater. Sol. Cells 192 (2019) 94–102, https://doi.org/10.1016/j.solmat.2018.12.019.
[28] B. Jo, D. Banerjee, Effect of solvent on specific heat capacity enhancement of binary molten salt-based carbon nanotube nanomaterials for thermal energy storage, Int. J. Therm. Sci. 98 (2015) 219–227, https://doi.org/10.1016/j.ijthermalsci.2015.07.020.
[29] Y. Yu, Y. Tao, Y.L. He, Molecular dynamics simulation of thermophysical properties of NaCl-SiO2 based molten salt composite phase change materials, Appl. Therm. Eng. 166 (2020), 114628, https://doi.org/10.1016/j.applthermaleng.2019.114628.
[30] H. Liu, Y. Li, Z. Fu, K. Li, M. Bauchy, Exploring the landscape of Buckingham potentials for silica by machine learning: soft vs hard interatomic forcefields, J. Chem. Phys. 152 (2020), 051101, https://doi.org/10.1063/1.5136041.
[31] S. Neyertz, D. Brown, J.O. Thomas, Molecular dynamics simulation of crystalline poly(ethylene oxide), the, J. Chem. Phys. 101 (1994) 10064–10073, https://doi.org/10.1063/1.467995.
[32] G. Qiao, M. Lasfargues, A. Alexiadis, Y. Ding, Simulation and experimental study of the specific heat capacity of molten salt based nanofluids, Appl. Therm. Eng. 111 (2017) 1517–1522, https://doi.org/10.1016/j.applthermaleng.2016.07.159.
[33] Y. Tian, J. Ding, X. Huang, K. Song, S.Q. Lu, H.R. Zheng, Development of novel interatomic potentials for simulation of rutile TiO2, Physica B 574 (2019), 311657, https://doi.org/10.1016/j.physb.2019.08.034.
[34] N. Baguer, V. Georgieva, L. Calderin, I.T. Todorov, S.V. Gils, A. Bogaerts, Study of the nucleation and growth of TiO2 and ZnO thin films by means of molecular dynamics simulations, J. Cryst. Growth 311 (2009) 4034–4043, https://doi.org/10.1016/j.jcrysgro.2009.06.034.
[35] Z. Li, L. Cui, B. Li, X. Du, Mechanism exploration of the enhancement of thermal energy storage in molten salt nanofluid, Phys. Chem. Chem. Phys. 23 (2021) 13181, https://doi.org/10.1039/D1CP00125F.
[36] P. Zhang, C. Zhu, D. Zhang, Q. Qiu, X. Ren, J. Liu, Molecular dynamic studies on MgO–Al2O3–SiO2 glass-ceramics, J. Mater. Res. 23 (2011) 2897–2908, https://doi.org/10.1557/JMR.2008.0367.
[37] J. Wang, J. Wu, Z. Sun, G. Lu, J. Yu, Molecular dynamics study of the transport properties and local structures of molten binary systems (Li, Na)Cl, (Li, K)Cl and (Na, K)Cl, J. Mol. Liq. 209 (2015) 498–507, https://doi.org/10.1016/j.molliq.2015.06.021.
[38] K.T. Karalis, D. Dellis, G.S. Antipas, A. Xenidis, Bona-fide method for the determination of short range order and transport properties in a ferro-aluminosilicate slag, Sci. Rep. 6 (2016) 30216, https://doi.org/10.1038/srep30216.
[39] P. Sahu, A.A. Pente, M.D. Singh, I.A. Chowdhri, K. Sharma, M. Goswami, S.M. Ali, K.T. Shenoy, S. Mohan, Molecular dynamics simulation of amorphous SiO2, B2O3, Na2O–SiO2, Na2O–B2O3, and Na2O–B2O3–SiO2 glasses with variable compositions and with Cs2O and SrO dopants, J. Phys. Chem. B 123 (2019) 6290–6302, https://doi.org/10.1021/acs.jpcb.9b03026.
[40] S. Gruenhut, D.R. MacFarlane, Molecular dynamics simulation of heavy metal fluoride glasses: comparison of Buckingham and BHM potentials, J. Non-Cryst. Solids 184 (1995) 356–362, https://doi.org/10.1016/0022-3093(94)00634-2.
[41] A.P. Thompson, H.M. Aktulga, R. Berger, D.S. Bolintineanu, W.M. Brown, P. S. Crozier, S.J. Plimpton, LAMMPS-a flexible simulation tool for particle-based materials modeling at the atomic, meso, and continuum scales, Comp Phys Commun 271 (2022), 108171, https://doi.org/10.1016/j.cpc.2021.108171.
[42] N. Galamba, C.A. Nieto de Castro, J.F. Ely, Molecular dynamics simulation of the shear viscosity of molten alkali halides, J. Phys. Chem. B 108 (2004) 3658–3662, https://doi.org/10.1021/jp036234x.
[43] M.P. Allen, D.J. Tildesley, Computer Simulation of Liquids: Second Edition, Oxford University Press, 2 ed., Oxford University Press, New York, 2017.
[44] X. Lv, A. Dong, Y. Dai, J. Wang, D. Shu, B. Sun, Temperature and concentration dependence of the physical properties and local structures of molten NaCl-KCl-LiCl mixtures, J. Mol. Liq. 229 (2017) 330–338, https://doi.org/10.1016/j.molliq.2016.12.091.
[45] W.G. Hoover, D.J. Evans, R.B. Hickman, A.J.C. Ladd, W.T. Ashurst, B. Moran, Lennard-Jones triple-point bulk and shear viscosities. Green-kubo theory, hamiltonian mechanics, and nonequilibrium molecular dynamics, Phys. Rev. A 22 (1980) 1690–1697, https://doi.org/10.1103/PhysRevA.22.1690.
[46] F. Lantelme, P. Turq, B. Quentrec, J.W.E. Lewis, Molecular physics: an international journal at the Interface between chemistry and physics, Mol. Phys. 28 (1974) 1537–1549, https://doi.org/10.1080/00268977400102791.
[47] Y. Lu, G. Zhang, J. Hao, J. Zhang, L. Chang, S. Yan, H. Zhang, Q. Cui, H, tan, molecular dynamics simulation of thermodynamic properties and local structure of Na2CO3-K2CO3 eutectic salt during phase transition, J. Energy Storage 43 (2021), 103221, https://doi.org/10.1016/j.est.2021.103221.
[48] G.J. Janz, Molten Salts Handbook, in: 2 ed., Academic Press, New York, 1967, pp. 184–211.
[49] W. Xie, J. Ding, G. Pan, Q. Fu, X. Wei, J. Lu, W. Wang, Heat and mass transportation properties of binary chloride salt as a high-temperature heat storage and transfer media, Sol. Energy Mater. Sol. Cells 209 (2020), 110415, https://doi.org/10.1016/j.solmat.2020.110415.
[50] X. Yang, M. Zhang, Y. Gao, J. Cui, B. Cao, Molecular dynamics study on viscosities of sub/supercritical n-decane, n-undecane and n-dodecane, J. Mol. Liq. 335 (2021), 116180, https://doi.org/10.1016/j.molliq.2021.116180.
[51] X. Yang, Y. Feng, J. Xu, J. Jin, Y. Liu, B. Cao, Numerical study on transport properties of the working mixtures for coal supercritical water gasification based power generation systems, Appl. Therm. Eng. 162 (2019), 114228, https://doi.org/10.1016/j.applthermaleng.2019.114228.
[52] G. Janz, F. Dampier, G. Lakshminarayanan, P. Lorenz, R. Tomkins, Molten Salts: Volume I. Electrical Conductance, Density, and Viscosity Data, NSRDS-NBS15, US Dept., Comm., Washington, 1968.
[53] W. Brockner, K. Grjotheim, T. Ohta, H.A. Øye, High-temperature viscometer for fluid liquids part II: viscosities of the alkali chlorides, berichte der bunsengesellschaft für physikalische, Chemie. 79 (1975) 344–347, https://doi.org/10.1002/bbpc.19750790406.
[54] N. Galamba, C.A. de Castro, J.F. Ely, Shear viscosity of molten alkali halides from equilibrium and nonequilibrium molecular-dynamics simulations, J. Chem. Phys. 122 (2005), 224501, https://doi.org/10.1063/1.1924706.
[55] J.O.M. Bockris, S.R. Richards, L. Nanis, Self-diffusion and structure in molten group II Chlorides1, J. Phys. Chem. 69 (1965) 1627–1637, https://doi.org/10.1021/J100889A031.
[56] R. Lenken, W. Uebelhack, A. Klemm, Selbstdiffusion in geschmolzenem LiCl / self-diffussion in molten LiCl, Z. Naturforsch. A 28 (1973) 881, https://doi.org/10.1515/zna-1973-0608.
[57] S.R. Becker, P.H. Poole, F.W. Starr, Fractional Stokes-Einstein and Debye-Stokes-Einstein relations in a network-forming liquid, Phys. Rev. Lett. 97 (2006), 055901, https://doi.org/10.1103/PhysRevLett.97.055901.
[58] W. Humphrey, A. Dalke, K. Schulten, VMD: visual molecular dynamics, J. Mol. Graph. 14 (1996) 33–38, https://doi.org/10.1016/0263-7855(96)00018-5.
[59] S.M.M. Rizvi, D. Shin, Mechanism of heat capacity enhancement in molten salt nanofluids int, J. Heat Mass Transf. 161 (2020), 120260, https://doi.org/10.1016/j.ijheatmasstransfer.2020.120260.
[60] M. Barisik, S. Atalay, A. Beskok, S. Qian, Size dependent surface charge properties of silica nanoparticles, J. Phys. Chem. C 118 (2014) 1836–1842, https://doi.org/10.1021/JP410536N.
[61] Z. Rao, K. Ye, H. Wang, S. Liao, Effects of interface layer on the thermophysical properties of solar salt-SiO2 nanofluids: a molecular dynamics simulation, Int. J. Energy Res. 45 (2021) 13323–13337, https://doi.org/10.1002/er.6659.
[62] X. Yang, D. Yu, B. Cao, Giant thermal rectification from single-carbon nanotube–graphene junction, ACS Appl. Mater. Interfaces 9 (2017) 24078–24084, https://doi.org/10.1021/acsami.7b04464.